



**Metastable Layered Lithium-rich Niobium and Tantalum
Oxides via Nearly Instantaneous Cation Exchange**

Journal:	<i>Faraday Discussions</i>
Manuscript ID	FD-ART-05-2024-000103.R1
Article Type:	Paper
Date Submitted by the Author:	23-Jul-2024
Complete List of Authors:	Ko, Sarah; University of California San Diego Dorrell, Jordan; University of Birmingham School of Metallurgy and Materials Morris, Andrew; University of Birmingham School of Metallurgy and Materials, Griffith, Kent; University of California San Diego

Metastable Layered Lithium-rich Niobium and Tantalum Oxides via Nearly Instantaneous Cation Exchange

Sarah L. Ko,¹ Jordan A. Dorrell,² Andrew J. Morris,² Kent J. Griffith^{1,3,*}

¹Department of Chemistry and Biochemistry, University of California, San Diego, California 92093, United States

²School of Metallurgy and Materials, University of Birmingham, Edgbaston, Birmingham B15 2TT, United Kingdom

³Program in Materials Science and Engineering, University of California, San Diego, California 92093, United States

*E-mail: k3griffith@ucsd.edu

Abstract

Lithium-rich early transition metal oxides are the source of excess removeable lithium that affords high energy density to lithium-rich battery cathodes. They are also candidates for solid electrolytes in all-solid-state batteries. These highly ionic compounds are sparse on phase diagrams of thermodynamically stable oxides, but soft chemical routes offer an alternative to explore new alkali-rich crystal chemistries. In this work, a new layered polymorph of Li_3NbO_4 with coplanar $[\text{Nb}_4\text{O}_{16}]^{12-}$ clusters is discovered through ion exchange chemistry. A more detailed study of the ion exchange reaction reveals that it takes place almost instantaneously, changing crystal volume by more than 22% within seconds. The transformation of coplanar $[\text{Nb}_4\text{O}_{16}]^{12-}$ in $\text{L-Li}_3\text{NbO}_4$ into the supertetrahedral $[\text{Nb}_4\text{O}_{16}]^{12-}$ clusters found in the stable cubic $\text{c-Li}_3\text{NbO}_4$ is also explored. Furthermore, this synthetic pathway is extended to access a new layered polymorph of Li_3TaO_4 . NMR crystallography with $^6,^7\text{Li}$, ^{23}Na , and ^{93}Nb NMR, X-ray diffraction, neutron diffraction, and first-principles calculations is applied to $A_3\text{MO}_4$ ($A = \text{Li, Na}$; $M = \text{Nb, Ta}$) to identify local and long-range atomic structure, to monitor the unusually rapid reaction progression, and to track the phase transitions from the metastable layered phases to the known compounds found by high-temperature synthesis. A mechanism is proposed whereby some sodium is retained at short reaction times, which then undergoes proton exchange during water washing, forming a phase with hydrogen bonds bridging the coplanar $[\text{Nb}_4\text{O}_{16}]^{12-}$ clusters. This study has implications for lithium-rich transition metal oxides and associated battery materials and for ion exchange chemistry in non-framework structures. The role of techniques that can detect light elements, local structure, and subtle structural changes in soft-chemical synthesis is emphasized.

Introduction

Lithium-rich compounds, oxides specifically, are emerging candidates for high-capacity lithium-ion battery electrode^{1–7} materials. On the cathode side, there are many examples of lithium-rich structures with compositions that fall on a tie-line intermediate between a lithium stoichiometric mid-to-late transition metal oxide (LiMO_2 ; $M = \text{Ni}^{3+}, \text{Co}^{3+}, \text{Mn}^{3+}, \text{Fe}^{3+}$) and a lithium-rich early transition metal oxide ($\text{Li}_2M^{4+}\text{O}_3, \text{Li}_3M^{5+}\text{O}_4, \text{Li}_4M^{6+}\text{O}_5$; $M = \text{Ti}^{4+}, \text{V}^{5+}, \text{Nb}^{5+}, \text{Mo}^{6+}$).^{5,8} Though fewer, there are also lithium-rich high-rate anodes such as $\text{Li}_3\text{V}_2\text{O}_5$ and $\text{Li}_3\text{Nb}_2\text{O}_5$.^{6,7} The structural phase-space of lithium-rich transition metal oxides, however, is relatively narrow. Most known phases feature a close-packed oxygen sublattice with octahedral cations yielding the disordered rocksalt structure (*e.g.*, aforementioned compositions, hydrothermal Li_3NbO_4 and Li_3TaO_4)^{8,9} or a cation-ordered rocksalt superstructure (*e.g.*, $\beta\text{-Li}_2\text{TiO}_3, \text{Li}_2\text{ZrO}_3, \text{c-Li}_3\text{NbO}_4, \alpha\text{- and } \beta\text{-Li}_3\text{TaO}_4, \text{Li}_4\text{MoO}_5, \text{Li}_4\text{WO}_5$)^{10–14}.

The known phase of Li_3NbO_4 (cubic, $\bar{I}43m$, ICSD 75264), here denoted *c-Li*₃NbO₄ for reasons that will become apparent, has an interesting crystal structure comprising octahedral NbO₆ that arrange in supertetrahedral clusters of $[\text{Nb}_4\text{O}_{16}]^{12-}$.^{12,13} Na₃NbO₄ (monoclinic, *C2/m*, ICSD 6116) also contains $[\text{Nb}_4\text{O}_{16}]^{12-}$ clusters, however, in this case they are co-planar.^{15–17} The unique arrangement of octahedral NbO₆ in Na₃NbO₄ thus gives rise to a layered compound that is denoted *L-Na*₃NbO₄. Moreover, unlike most of the lithium compounds, it does not feature a close-packed oxygen sublattice. A related situation arises in the *A*₃TaO₄ (*A* = Li, Na). There are two known high-temperature forms of Li_3TaO_4 , the α and β polymorphs, both featuring chains of TaO₆ octahedra in a lattice of close-packed oxygen.^{18–20} Na₃TaO₄ is isostructural with Na₃NbO₄.^{14,21}

In the context of exploratory synthesis toward materials relevant for next-generation batteries, it is worthwhile to pursue lithium-rich transition metal oxides with unique underlying crystal structures. Ion exchange has been successfully applied as a synthetic route to create a variety of new or low-defect lithium metal oxides.^{22–27} The mild conditions of ion exchange, relative to high-temperature ceramic methods, favor topotactic reactions that lead to metastable products with complete or systematic partial replacement²⁸ of the original guest cations. Typical host structures are interconnected frameworks or 2D layered solids. Of the non-interconnected hosts that undergo ion exchange, polyoxometalates (POMs) with large, well-

defined cluster anions are perhaps the best known.²⁹ Less explored is the chemistry of small clusters found among the alkali-rich early transition metal oxides.

In this work, we synthesized layered L-Li₃NbO₄ with zero-dimensional (0D) coplanar [Nb₄O₁₆]¹²⁻ anionic clusters and a non-close-packed oxygen sublattice via cation exchange in a molten salt flux. An NMR crystallography approach combining X-ray and neutron diffraction, ⁶Li, ⁷Li, ²³Na, and ⁹³Nb solid-state NMR, and *ab initio* structure and spectral calculations was adopted to characterize L-Li₃NbO₄ and its relationship to related phases such as c-Li₃NbO₄ and L-Na₃NbO₄. The combination of experimental and computational solid-state NMR spectra is particularly powerful here owing to the global symmetry and local distortion differences amongst the various phases. After discovering that the ion exchange reaction to form L-Li₃NbO₄ occurs in a matter of seconds, diffraction, NMR, and DFT were again combined to track the composition and structure evolution and the ion exchange mechanism as a function of reaction time. Finally, we show that this synthetic and characterization methodology are transferrable through the realization of another new phase, layered L-Li₃TaO₄.

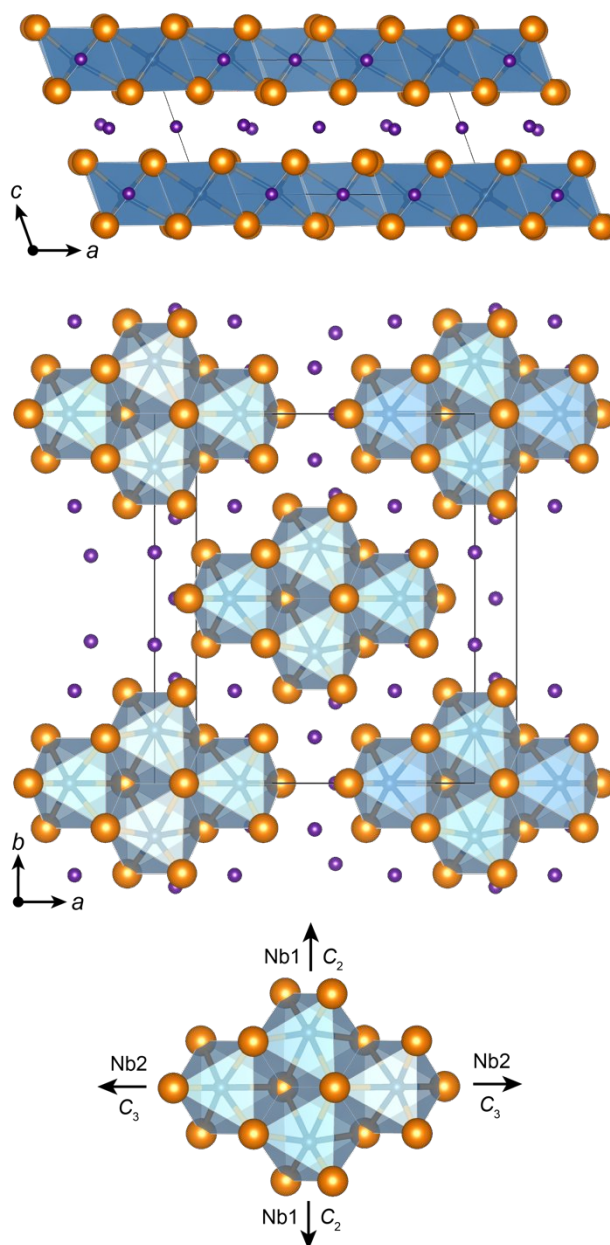


Figure 1. Crystal structure of layered Li₃NbO₄ synthesized topotactically from Na₃NbO₄. Planar [Nb₄O₁₆]¹²⁻ clusters align in the *ab* plane and are separated by a sea of alkali cations. The bottom panel depicts the direction and symmetry of the SOJT distortions of niobium atoms within their respective octahedra. Lithium atoms in purple, NbO₆ octahedra in blue, and oxygen atoms in orange.

Experimental

Reagents and synthesis. The stable high-temperature phases of L-Na₃NbO₄, L-Na₃TaO₄, c-Li₃NbO₄, and m-Li₃TaO₄ were synthesized in approximately 1 g batches according to previously reported high-temperature solid-state methods.^{30,15} T-Nb₂O₅ (99.85%, D₅₀ = 450 nm, CBMM) or L-Ta₂O₅ (99.9%, MSE Supplies) were ground with Li₂CO₃ (anhydrous, ≥ 99.0%, Sigma Aldrich) or Na₂CO₃ (anhydrous, 99.95%, Sigma Aldrich) in stoichiometric amounts with a mortar and pestle and pressed into a pellet at 300 MPa with a 13-mm-diameter stainless steel die. The pellet was heated in a magnesia crucible with a magnesia cover at 850 °C for 12 hours for the sodium compounds or 1000 °C for 12 hours for the lithium compounds. Ion exchange from L-Na₃MO₄ to L-Li₃MO₄ (*M* = Nb, Ta) was performed by grinding together 200 mg of the layered sodium compound with LiNO₃ (≥ 98.5%, Sigma Aldrich) in a 1:10 Na₃MO₄:salt mass ratio. The mixture was heated in an alumina crucible at 335 °C for up to 12 h. After heating, the salt was dissolved with DI water and the final product was recovered by vacuum filtration over a PVDF membrane (Durapore, 0.22 μm, hydrophilic). For the time-stepped ion exchange, the salt was pre-heated to 335 °C before L-Na₃NbO₄ was added into the molten salt inside the crucible. The sample and flux reacted for variable times ranging from 30 seconds to 12 hours before being quenched in cold water.

Powder X-ray diffraction (PXRD) and scanning electron microscopy (SEM). Powder X-ray diffraction was performed with a Bruker D8 Advance powder diffractometer using Cu K α radiation ($\lambda = 1.54 \text{ \AA}$) with operating voltage of 40 kV and a current of 40 mA. X-ray diffraction powder patterns were recorded from 5–90° 2θ with a step size of 0.020° at 0.4 seconds per step. Scanning electron microscopy was performed with an FEI Apreo SEM operating with a beam current of 0.40 nA and a voltage of 10 kV.

Neutron powder diffraction. Time-of-flight neutron powder diffraction (TOF-NPD) data were measured on the POWGEN diffractometer at the Spallation Neutron Source (SNS) at Oak Ridge National Laboratory.³¹ The neutron samples comprised 4.242 g of L-Na₃NbO₄ loaded into an 8-mm-diameter cylindrical vanadium can and 1.923 g of Li₃NbO₄ loaded into a 6-mm-diameter cylindrical vanadium can. Both cans were loaded into the POWGEN sample changer (PAC) and measured at 20 K and 300 K. Data were collected on POWGEN detector bank 1 with a center wavelength of 0.8 Å (*d*-spacing range 0.1–8 Å) for Li₃NbO₄ at 20 K and detector bank 2 with a center wavelength of 1.5 Å (*d*-spacing range 0.5–12.5 Å) for all other measurements. Data collection times for L-Na₃NbO₄ at 20 K, L-Na₃NbO₄ at 300 K, L-Li₃NbO₄

at 20 K, and L-Li₃NbO₄ at 300 K were 44, 86, 150, and 58 mins, respectively. Rietveld refinements were performed in GSAS-II.³² The large sample of L-Na₃NbO₄ prepared for neutron diffraction contained 1 wt.% Na₂CO₃ while the L-Li₃NbO₄ sample contained 1 wt.% Li₂CO₃; both could be observed by their characteristic (110) reflections at $Q = 1.400 \text{ \AA}^{-1}$ and 1.509 \AA^{-1} , respectively. The neutron wavevector Q is defined as $Q = 2\pi/d$.

Particle size analysis. Particle size distributions were recorded with a Shimadzu SALD-7500nano particle size analyzer. Each powder was dispersed in isopropyl alcohol at a concentration of 1 mg/mL, sonicated, and measured in a quartz cell (Batch Cell SALD-BC75) with a 405 nm laser. The refractive indices for these measurements were calculated with methods by Kinoshita.³³

Solid-state NMR experiments. All NMR measurements were performed at 9.4 T on a Bruker Ascend 400 magnet and Bruker Avance NEO NMR spectrometer with a 5.0 mm or 1.6 mm Phoenix HX probe. Samples were fully packed into zirconia rotors with PCTFE and polyimide (5 mm) or polyimide and polyamide-imide (1.6 mm) caps. 1D measurements used a direct pulse–acquire pulse sequence and a recycle delay time of $\geq 5 \times T_1$. T_1 (longitudinal) relaxation was measured with a saturation-recovery pulse sequence with up to 37 delay times spanning 10 μ s up to 10,000 s, equally spaced in $\log_{10}(t)$. T_1 relaxation data, recycle delays, and the number of FIDs recorded for each experiment are reported in Supplementary Information Figure S1, Table S1, and Table S2. NMR data processing and lineshape fits were performed with Bruker TopSpin 4.3.0 and DMfit.³⁴

This work uses the Haeberlen convention for NMR tensors. With the principal components of the shift tensor ordered such that $|\delta_{ZZ} - \delta_{iso}| \geq |\delta_{XX} - \delta_{iso}| \geq |\delta_{YY} - \delta_{iso}|$, the isotropic shift $\delta_{iso} = \frac{\delta_{XX} + \delta_{YY} + \delta_{ZZ}}{3}$, chemical shift anisotropy $\delta_{aniso} = \delta_{ZZ} - \delta_{iso}$, and the chemical shift asymmetry $\eta_{CS} = \frac{\delta_{YY} - \delta_{XX}}{\delta_{ZZ} - \delta_{iso}}$. The above definition of δ_{aniso} is sometimes referred to as the reduced anisotropy, which is equal to 2/3 of the ‘full’ anisotropy $\Delta\delta = \delta_{ZZ} - \frac{\delta_{XX} + \delta_{YY}}{2}$ used by some authors and programs. With the principal components of the electric field gradient (EFG) tensor at the nucleus ordered such that $|V_{ZZ}| \geq |V_{YY}| \geq |V_{XX}|$, the quadrupolar coupling constant C_Q is defined by the nuclear quadrupole moment Q , the largest principal component of the EFG V_{ZZ} , the electric charge e , and Planck’s constant h according to $C_Q = \frac{eQ \cdot V_{ZZ}}{h}$. The quadrupolar asymmetry parameter η_Q is defined as $\eta_Q = \frac{V_{XX} - V_{YY}}{V_{ZZ}}$. The relative orientations of the chemical

shift and quadrupolar tensors are defined by a set of Euler angles α , β , γ defined here in the (ZYZ) Rose convention as implemented in MagresView 2.0.³⁵

⁶Li and ⁷Li NMR. ⁶Li and ⁷Li experiments were measured at Larmor frequencies of 58.88 and 155.51 MHz, respectively, with the sample rotated about the magic angle at a frequency of 10 or 20 kHz (no temperature regulation). For ⁶Li, spectra were acquired using a 90° pulse of 6.25 μ s (40 kHz) in the 5 mm probe or 2.70 μ s (93 kHz) in the 1.6 mm probe. For ⁷Li, spectra were acquired using a 90° pulse of 6.10 μ s (41 kHz) in the 5 mm probe or 2.15 μ s (116 kHz) in the 1.6 mm probe. Both ⁶Li and ⁷Li were referenced with respect to 9.7 m LiCl in D₂O at 0 ppm.³⁶

²³Na NMR. ²³Na spectra were measured at the Larmor frequency of 105.84 MHz and 10 kHz (1D) or 12.5 kHz MAS (MQMAS). 1D spectra were acquired with a 45° pulse of 1.50 μ s (83 kHz). A three-pulse *z*-filtered MQMAS³⁷ experiment was conducted with 9 μ s, 3 μ s, and 28 μ s pulses. The MQMAS experiment used a recycle delay of 18 s, 96 FIDs per row, and 200 rows (96 h experimental time). ²³Na was referenced to solid NaCl at 7.21 ppm.³⁸ The MQMAS spectrum is referenced according to the Wimperis convention.³⁹

⁹³Nb NMR. ⁹³Nb spectra were measured at a Larmor frequency of 97.83 MHz under magic angle rotation at a frequency of 30 or 39 kHz. 1D spectra were acquired with a pulse of 0.4 μ s, which is estimated to be a 20° pulse based on the liquid 90° pulse of nearby ¹³C. ⁹³Nb spectra of several samples were recorded with pulses varying from 0.25 to 0.75 μ s and the observed lineshapes were not sensitive to these variations. ⁹³Nb was referenced to solid LiNbO₃ at -1004 ppm (Supplementary Figure S2).⁴⁰

DFT Calculations

All structures reported in this work have been geometry optimised using forces and stresses derived from density-functional theory (DFT) calculations as implemented in the CASTEP v21 planewave DFT code.⁴¹ NMR parameters were also calculated using CASTEP and the gauge-including projector augmented wave (GIPAW) method.⁴² Calculations were performed using a Monkhorst–Pack^{43,44} *k*-point grid with a spacing of $2\pi \times 0.03 \text{ \AA}^{-1}$ and a planewave cut-off energy of 1000 eV. CASTEP's on-the-fly ultrasoft pseudopotentials from CASTEP v21 were used with the PBE¹² exchange–correlation functional as implemented in CASTEP.

Results and Discussion

Synthesis and structure. Given the interesting relationship between the supertetrahedral $[M_4O_{16}]^{12-}$ arrangement of octahedra in the stable cubic phase $c\text{-Li}_3\text{NbO}_4$ and the coplanar $[M_4O_{16}]^{12-}$ cluster of the stable layered phase $L\text{-Na}_3\text{NbO}_4$, we set out to explore whether the layered polymorph of Li_3NbO_4 could be realized via ion exchange. Host structures capable of topotactic ion exchange typically feature 2D or 3D connectivity, so there was little precedence for the process in 0D cluster compounds such as $L\text{-Na}_3\text{NbO}_4$.

$L\text{-Na}_3\text{NbO}_4$ was prepared at 850 °C from Nb_2O_5 and Na_2CO_3 . The sample was phase pure with the exception of a small quantity of NaNbO_3 , typically 2–3%, that could have formed during the synthesis or by reaction of the product with atmospheric carbon dioxide. In the initial ion exchange reaction, $L\text{-Na}_3\text{NbO}_4$ was left in a flux of molten LiNO_3 for 12 h. The diffraction peaks of the ion exchanged product, whilst substantially broadened, could be indexed in the same unit cell with lattice parameters a, b, c contracted by approximately 7%, 8%, and 10%, respectively (Figure 2).

Sodium and lithium are not easily differentiated by X-rays in a compound where the scattering is dominated by niobium so two additional characterization routes were pursued: neutron diffraction and solid-state NMR spectroscopy. Multigram samples of $L\text{-Na}_3\text{NbO}_4$ and $L\text{-Li}_3\text{NbO}_4$ were prepared and measured at 20 K and 300 K with time-of-flight neutron diffraction on the POWGEN beamline at Oak Ridge National Laboratory (Supplementary Information Figure S3). Rietveld refinement of $L\text{-Na}_3\text{NbO}_4$ was carried out with 20 K and 300 K datasets, allowing the lattice parameters, atomic positions, and isotropic displacement parameters to refine freely (Figure 3a, Supplementary Information Figure S4). The results of these fits are given in Table 1 and as crystallographic information files in the Supplementary Information. $L\text{-Na}_3\text{NbO}_4$ was used as the starting point for the refinement of $L\text{-Li}_3\text{NbO}_4$. First, the lattice parameters were adjusted by hand to roughly match the peak positions, which changed by too much during the ion exchange to be handled by unassisted least-squares refinement (Figures 2–3, Supplementary Information Figure S4). The room-temperature unit

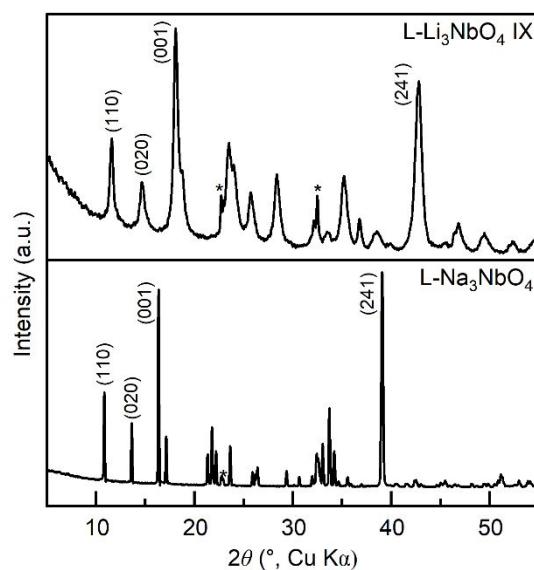


Figure 2. X-ray diffraction patterns of layered Na_3NbO_4 (bottom) and Li_3NbO_4 after 12 h of ion exchange in a molten lithium salt (top). Some of the most prominent reflections are labeled. Asterisks denote observed NaNbO_3 reflections.

cell volume of L-Na₃NbO₄ decreased by 22.6% upon ion exchange with lithium. Broadened line shapes, which likely come from strain⁴⁵ since the particle size did not change significantly during ion exchange (Supplementary Information Figures S5–S6), were accounted for in the refinement by the isotropic strain parameter and instrumental broadening terms. In the structure model of L-Li₃NbO₄, lithium ions were initially placed on the sodium positions of L-Na₃NbO₄. The positions were refined followed by constrained isotropic displacement parameter refinement (one B_{iso} per atomic species), which yielded a good fit to the data (Figure 3b, Supplementary Information Figure S4b). The presence of lithium was also supported by clearly defined pockets of negative nuclear density in Fourier difference maps when any one of the lithium atoms was removed. DFT geometry optimizations of L-Na₃NbO₄ and L-Li₃NbO₄ yielded close agreement with the experimental crystal structures (Table 1, Supplementary Table S3).

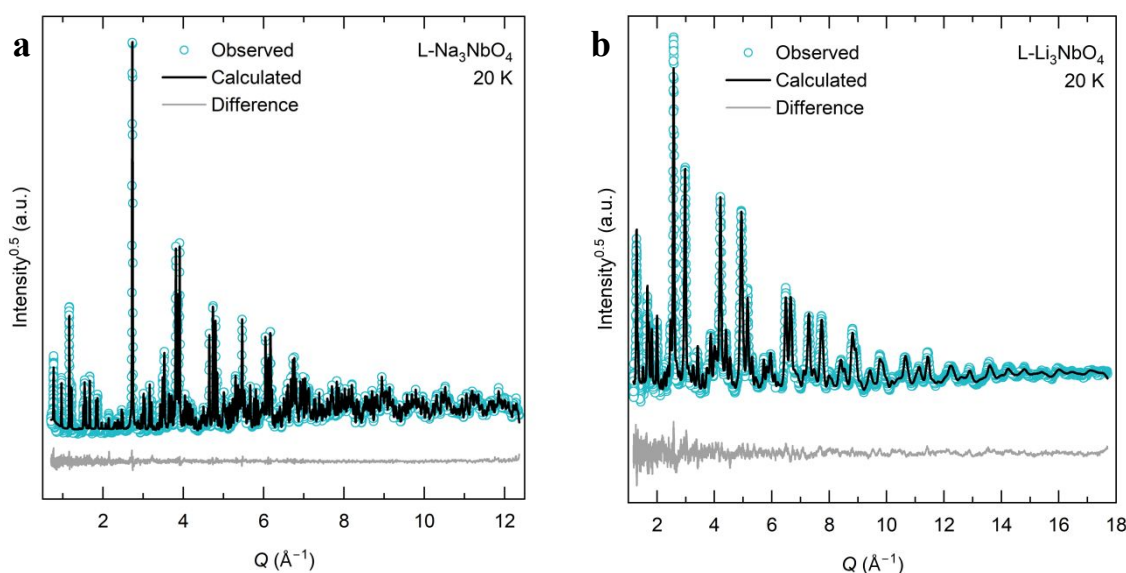


Figure 3. Neutron powder diffraction patterns and Rietveld refinement fits of (a) L-Na₃NbO₄ and (b) L-Li₃NbO₄. Square-root intensity is shown to better depict data to high Q .

Table 1. Lattice parameters of L-Na₃NbO₄ and L-Li₃NbO₄ from refinement of the structures with neutron powder diffraction data.

Layered $C2/m$	300 K			20 K		
	Na ₃ NbO ₄	Li ₃ NbO ₄	Δ (%)	Na ₃ NbO ₄	Li ₃ NbO ₄	Δ (%)
a (Å)	11.1218(4)	10.39(2)	−6.6	11.0923(5)	10.36(2)	−6.6
b (Å)	13.00203(7)	11.944(3)	−8.1	12.9711(1)	11.904(3)	−8.2
c (Å)	5.7529(1)	5.202(4)	−9.6	5.7350(2)	5.179(4)	−9.7
β (°)	109.4905(6)	109.91(2)		109.4294(7)	109.83(2)	
Volume (Å ³)	784.233(6)	606.7(1)	−22.6	778.16(2)	601.0(1)	−22.8

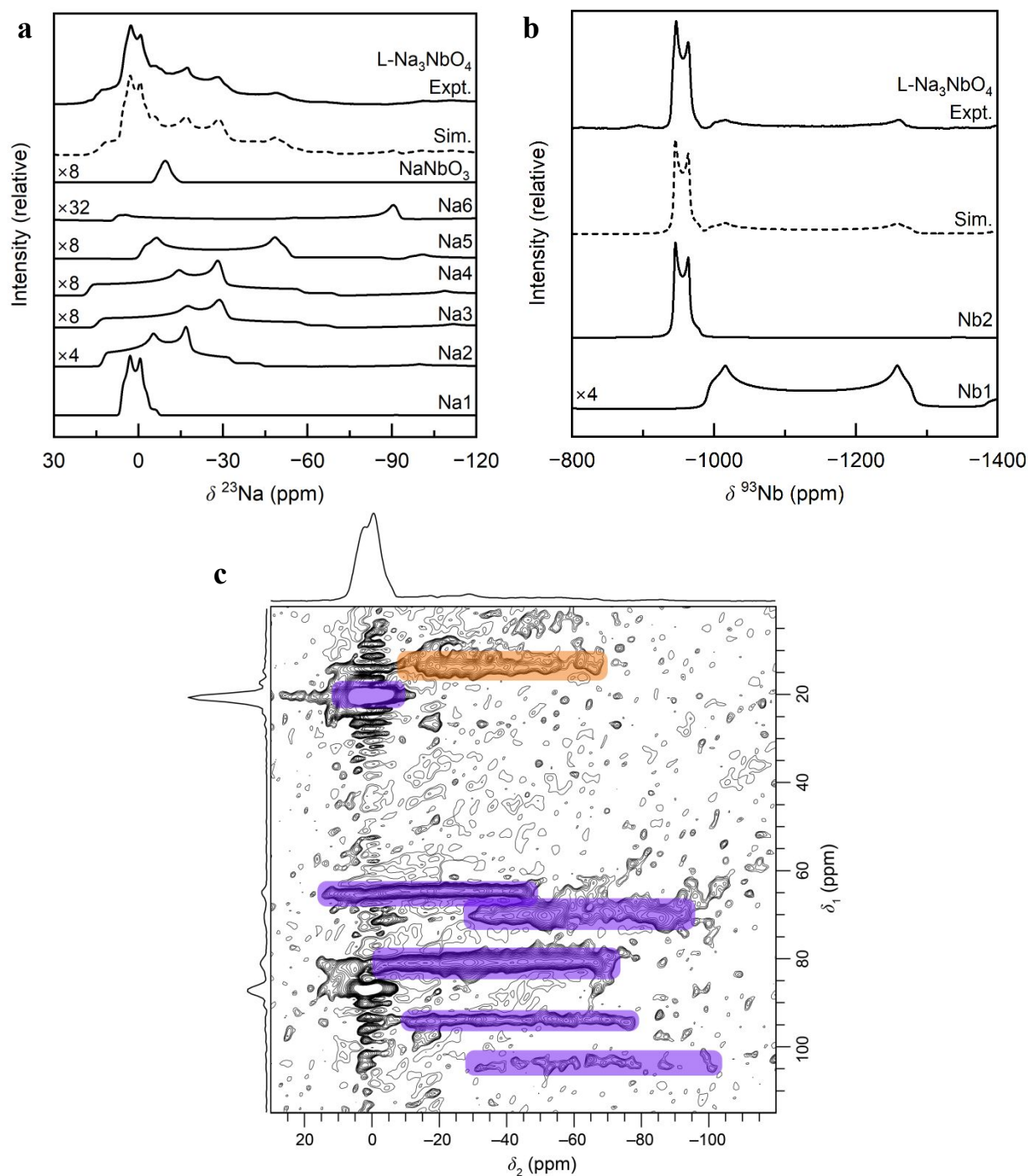


Figure 4. (a) ^{23}Na 1D, (b) ^{93}Nb 1D, and (c) ^{23}Na MQMAS NMR of $\text{L-Na}_3\text{NbO}_4$ at 9.4 T. The simulated ^{23}Na spectrum in (a) includes contributions from the six unique sodium sites in the crystal structure and the NaNbO_3 impurity. Broader sites in (a,b) are scaled up in intensity, as denoted, to better show their lineshapes. The purple boxes in (c) correspond to the six crystallographic sodium sites in $\text{L-Na}_3\text{NbO}_4$ while the orange box corresponds to NaNbO_3 . ^{23}Na 1D and MQMAS were measured at 10 and 12.5 kHz MAS, respectively, and ^{93}Nb was measured at 38.5 kHz MAS.

Solid-state NMR spectroscopic analysis of the ion exchange reaction also started with $\text{L-Na}_3\text{NbO}_4$. The crystal structure of $\text{L-Na}_3\text{NbO}_4$ features six sodium and two niobium atoms in the asymmetric unit. ^{23}Na and ^{93}Nb NMR of $\text{L-Na}_3\text{NbO}_4$, simulated with parameters refined

from planewave DFT calculations, give good agreement between experiment and theory (Figure 4, Tables 2–3). Measurement of ^{23}Na NMR after the ion exchange process gives not only a quantitative measure of the extent of the ion exchange but also yields phase-specific information on the residual sodium. The only sodium remaining in the washed, ion-exchanged sample, L- Li_3NbO_4 , was the 2–3% NaNbO_3 that was present in the original L- Na_3NbO_4 precursor (Figure 5a). This NaNbO_3 is a mixture of two polymorphs, *Pbcm* and *P2₁ma*, fit on the basis of the detailed work by Johnston et al⁴⁶ (Table 2). NaNbO_3 apparently does not undergo ion exchange in molten lithium nitrate within 12 h at 335 °C.

Table 2. ^{23}Na NMR of Na_3NbO_4 and NaNbO_3 .

Site	<u>calculated</u>					<u>experimental^a</u>			
	σ_{iso} (ppm)	δ_{aniso} (ppm)	η_{CS}	C_Q (MHz)	η_Q	δ_{iso} (ppm)	C_Q (MHz)	η_Q	
L- Na_3NbO_4	Na1	556.8	10.6	0.11	1.529	0.41	6.7(5)	1.55(10)	0.41(1)
	Na2	548.0	−22.6	0.79	−3.133	0.57	15(1)	3.1(2)	0.57(3)
	Na3	544.5	−14.0	0.32	−3.726	0.72	16(1)	3.7(2)	0.72(1)
	Na4	542.4	−11.1	0.92	−3.801	0.62	29(1)	3.8(2)	0.68(4)
	Na5	551.0	−8.5	0.55	−4.334	0.08	10(1)	4.2(2)	0.10(2)
	Na6	551.7	−35.0	0.35	5.668	0.62	9(5) ^b	5.5(5) ^{b,c}	n/a ^{b,c}
NaNbO_3 <i>Pbcm</i>	Na1						−1.3(5)	2.1(1)	0.01(5)
	Na2						−5.7(5)	1.0(1)	0.8(2)
NaNbO_3 <i>P2₁ma</i>	Na1						−2.1(5)	2.1(1)	0.9(1)
	Na2						−5.5(5)	1.1(1)	0.7(2)

^a‘Experimental’ values obtained by first simulating the GIPAW calculated values and then refining the isotropic chemical shift and the quadrupolar coupling magnitude and asymmetry to obtain a best-fit of the simulation to the experimental data. Error estimates are based on evaluation of the local minimum fit and do not exclude the possibility that this is not the global minimum fit given the degree of ^{23}Na spectral overlap. ^bDetermined from the $\delta_i \sim 105$ ppm low-intensity site observed in the MQMAS spectrum. ^c C_Q was calculated from $P_Q = C_Q(1 + \eta_Q^2/3)^{1/2}$ using the GIPAW calculated value of η_Q .

Table 3. ^{93}Nb NMR of Li_3NbO_4 and Na_3NbO_4 .

Site	<u>calculated</u>					<u>experimental^a</u>			
	σ_{iso} (ppm)	δ_{aniso} (ppm)	η_{CS}	C_Q (MHz)	η_Q	δ_{iso} (ppm)	C_Q (MHz)	η_Q	
c- Li_3NbO_4	Nb1	313	−128	0.00	−13.2	0.00	−977(5)	12.4(2)	0.12(2)
L- Li_3NbO_4	Nb1	303	−129	0.28	27.3	0.41	−998(10)	27(2)	0.41(5)
	Nb2	334	124	0.24	−11.9	0.08	−977(5)	12(2)	0.08(5)
L- Na_3NbO_4	Nb1	223	−93	0.02	42.9	0.02	−924(10)	39.0(5)	0.08(3)
	Nb2	247	108	0.51	17.4	0.00	−938(5)	10.9(2)	0.00(2)

^a'Experimental' values obtained by first simulating the GIPAW calculated values and then refining the isotropic chemical shift and the quadrupolar coupling magnitude and asymmetry to obtain a best-fit of the simulation to the experimental data.

The ⁹³Nb MAS NMR spectrum of L-Li₃NbO₄ is in good agreement with the parameters calculated from DFT on the basis of the structure refined from neutron diffraction data (Figure

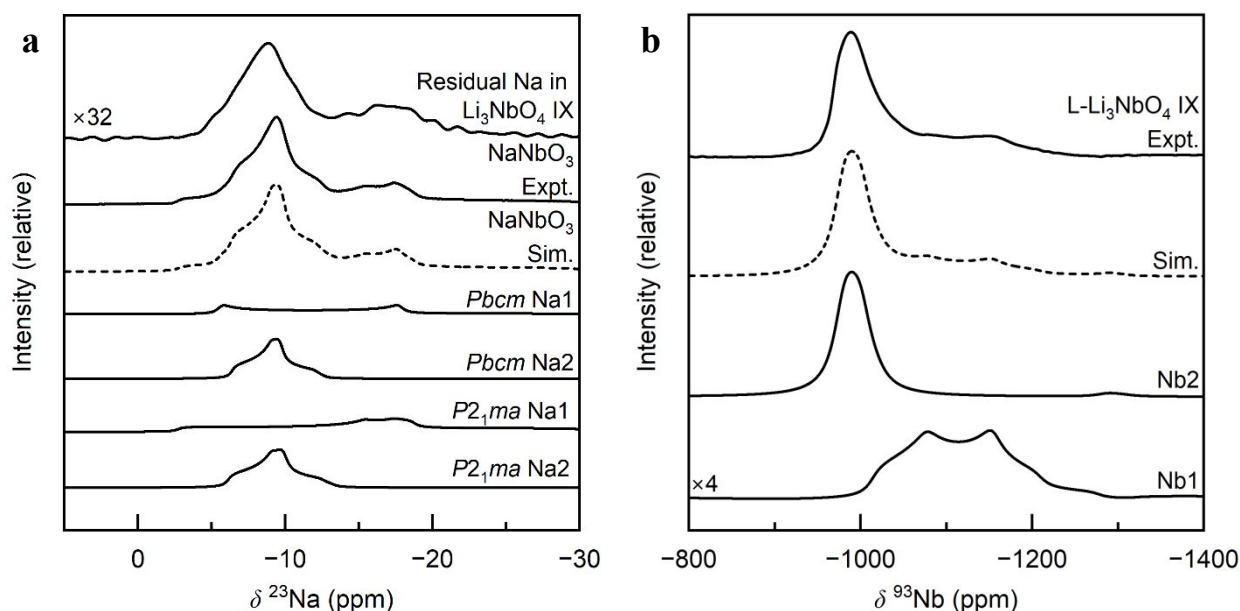


Figure 5. (a) ²³Na and (b) ⁹³Nb NMR of L-Li₃NbO₄ at 9.4 T. The simulated ²³Na spectrum is made up of two polymorphs of the NaNbO₃ impurity present in the precursor L-Na₃NbO₄. ²³Na was measured at 10 kHz MAS and ⁹³Nb was measured at 30 kHz MAS. The residual NaNbO₃ in (a) and the broader Nb2 site in (b) are scaled up in intensity, as denoted, to better show their lineshapes.

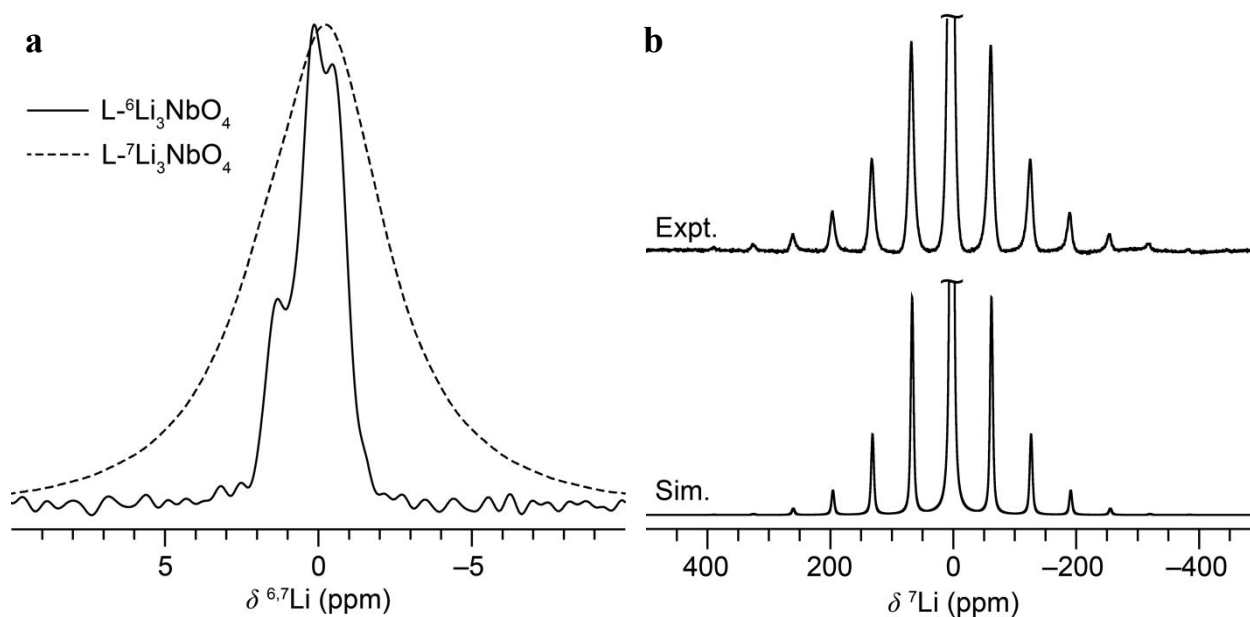


Figure 6. (a) ^{6,7}Li centerband spectra and (b) ⁷Li spinning sideband manifold of L-Li₃NbO₄ at 9.4 T and 10 kHz MAS. Spectra in (a) are intensity normalized. Centerband truncated in (b). Sideband simulation performed with the calculated ⁷Li C_Q and η_Q parameters for L-Li₃NbO₄.

5b, Table 3). The ^{93}Nb signal from NaNbO_3 is not obvious in $\text{L-Li}_3\text{NbO}_4$ as it is only a minor component (2–3%) and its centerband overlaps with a feature of the Nb1 site of $\text{L-Li}_3\text{NbO}_4$ (Supplementary Figure S2). The ^{93}Nb spectrum of $\text{L-Li}_3\text{NbO}_4$ differs from that of $\text{c-Li}_3\text{NbO}_4$ (Supplementary Figure S7, Table 3) in that the former exhibits two sites while the latter has only one crystallographically unique niobium position. The utility of the quadrupolar coupling parameters becomes apparent here. C_Q and η_Q of the octahedral ^{93}Nb site in $\text{c-Li}_3\text{NbO}_4$ are statistically identical to those of the octahedral Nb2 site of $\text{L-Li}_3\text{NbO}_4$; both of these sites experience C_3 off-centering distortions toward an octahedral face.⁴⁷ Contrast this with the octahedral Nb1 site of $\text{L-Li}_3\text{NbO}_4$ that experiences a C_2 off-centering distortion toward the O2 atoms and has a significantly different quadrupolar NMR lineshape (Figure 1, Figure 5b, Supplementary Figure S7, Table 3). In both $\text{c-Li}_3\text{NbO}_4$ and $\text{L-Li}_3\text{NbO}_4$, these distortions maximize Nb–Nb interatomic distances within the clusters.

^6Li and ^7Li NMR were also measured after the ion exchange reaction. The ^7Li spectrum shows a single isotropic resonance at 0.1 ppm, which is substantially broadened by homonuclear dipolar coupling that is not effectively removed by magic-angle spinning in this lithium-rich compound (Figure 6a). However, the spinning sideband manifold of ^7Li arising from quadrupolar-broadened $\pm 3/2$ to $\pm 1/2$ satellite transitions provides a useful dataset to compare against the calculated nuclear quadrupolar coupling constants for $\text{L-Li}_3\text{NbO}_4$, which range from 20 to 100 kHz (Figure 6b, Table 4). A simulation of the ^7Li spinning sideband manifold at 10 kHz MAS rate with the parameters for $\text{L-Li}_3\text{NbO}_4$ from Table 4 slightly underestimates the experimental manifold but is a reasonable fit (Figure 6b), particularly considering the high strain indicated by the diffraction data. The ^6Li NMR spectrum presents a much higher resolution lineshape (Figure 6a). As a nucleus, ^6Li has a natural abundance of 7.6% and a gyromagnetic ratio that is 38% of ^7Li . As a result of these nuclear properties, ^6Li features NMR spectra with minimal residual dipolar broadening. Based on the crystal structure and CASTEP NMR calculations, $\text{L-Li}_3\text{NbO}_4$ is expected to have six lithium sites with a chemical shift range of 2.2 ppm. Experimentally, three environments were resolved with chemical shifts of 1.33 ppm, 0.14 ppm, -0.46 ppm and a range of 1.79 ppm. Three of the sites have calculated shieldings within 0.07 ppm and appear at the center of the range, which is consistent with the experimental lineshape. Lithium NMR of $\text{L-Li}_3\text{NbO}_4$ can be compared to that of $\text{c-Li}_3\text{NbO}_4$ shown in Figure 7. ^6Li and ^7Li NMR spectra of $\text{c-Li}_3\text{NbO}_4$ each feature a single symmetric lineshape centered at -0.1 ppm (Figure 7a). The ^7Li spinning sideband

manifold can be well simulated with a C_Q of 35 kHz as indicated by the CASTEP DFT calculations (Figure 7b).

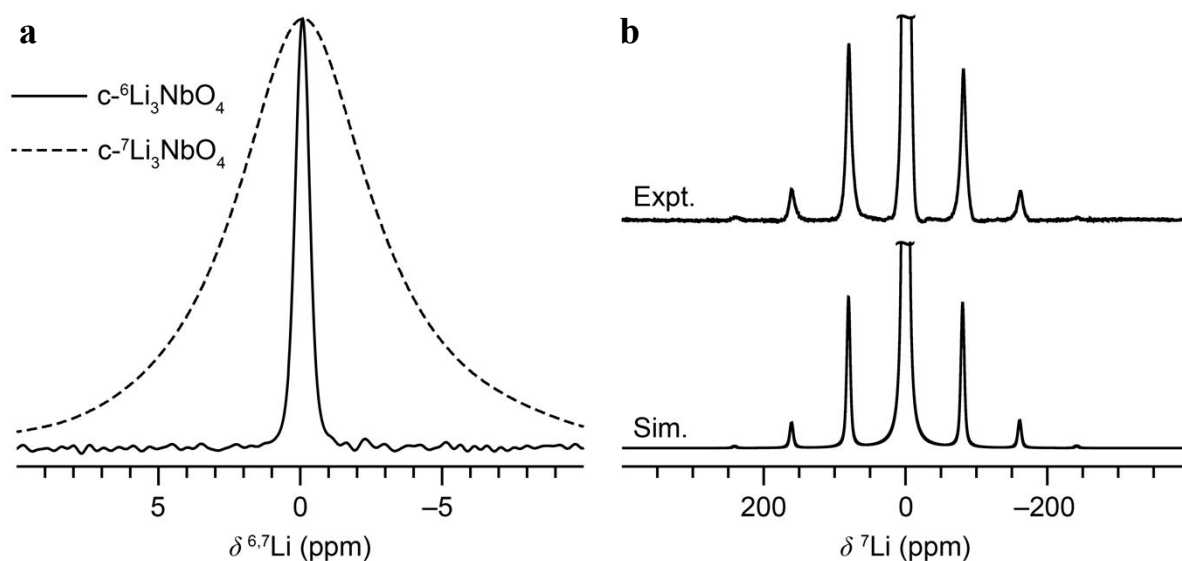


Figure 7. (a) $^{6,7}\text{Li}$ centerband spectra and (b) ^7Li spinning sideband manifold of $c\text{-Li}_3\text{NbO}_4$ at 9.4 T and 12.5 kHz MAS. Spectra in (a) are intensity normalized. Centerband truncated in (b). Sideband simulation performed with the calculated ^7Li C_Q and η_Q parameters for $c\text{-Li}_3\text{NbO}_4$.

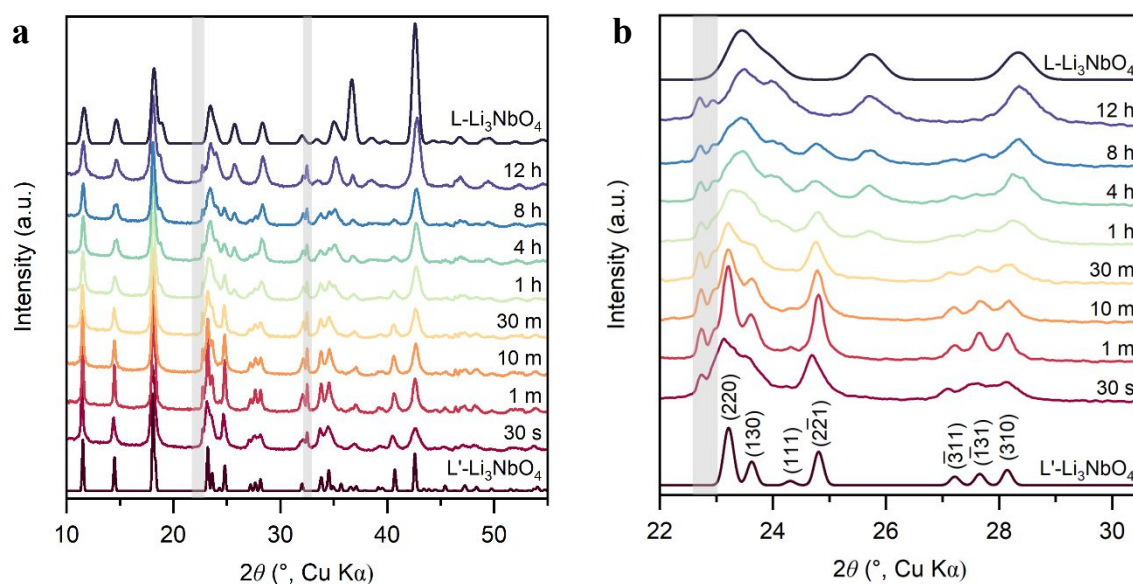


Figure 8. (a) X-ray diffraction patterns of $L\text{-Li}_3\text{NbO}_4$ as a function of ion exchange time in molten LiNO_3 . (b) Diffraction pattern region from $22\text{--}30.5^\circ$ 2θ highlighting the time evolution of peak positions and lineshapes. The shaded region in each figure denotes the position of NaNbO_3 impurity reflections. The top and bottom curves in each figure are calculated diffraction patterns; intermediate curves are experimental data. See main text for an explanation of $L'\text{-Li}_3\text{NbO}_4$.

Table 4. $^{6,7}\text{Li}$ NMR of Li_3NbO_4 .

Site	σ_{iso} (ppm)	δ_{aniso} (ppm)	η_{CS}	C_Q (kHz) ^a	η_Q
------	----------------------	------------------------	-------------	--------------------------	----------

c-Li ₃ NbO ₄	Li1	89.70	-1.36	0.67	-35.2	0.40
	Li1	88.89	-0.57	0.82	20.5	0.55
	Li2	90.14	-2.09	0.87	-47.5	0.29
L-Li ₃ NbO ₄	Li3	90.11	-0.35	0.79	55.8	0.99
	Li4	91.07	0.88	0.47	-46.7	0.11
	Li5	90.18	0.72	0.91	55.9	0.10
	Li6	89.59	-3.47	0.47	-99.0	0.69

^aC_Q for ⁷Li nucleus. ⁶Li C_Qs are scaled by $Q(^6\text{Li})/Q(^7\text{Li}) = 0.808/40.1$.⁴⁸

Ion exchange timescale and mechanism. In order to better understand the ion exchange process from L-Na₃NbO₄ to L-Li₃NbO₄, a series of time-resolved experiments were carried out by quenching the ion-exchange reaction after 30 s to 12 h. At each time point, XRD, ⁶Li, ⁷Li, ²³Na, and ⁹³Nb NMR were measured. Unexpectedly, it was immediately apparent from the diffraction patterns that L-Li₃NbO₄ formed after a matter of seconds and no residual L-Na₃NbO₄ peaks were detected (Figure 8).

Before discussing this data further, an important caveat is that Na₃NbO₄ is not stable in water and decomposes to an unknown phase suspected to be a hydrate with its two strongest diffraction peaks at *d*-spacings of 7–8 Å (Supplementary Figure S8). To consider the role of water-washing on the products, diffraction and NMR data were also collected on an unwashed sample after 1 min of ion exchange (Figure 9). There is a large background signal from the (Li,Na)NO₃ flux but the characteristic diffraction peaks of L-Li₃NbO₄ are apparent while no L-Na₃NbO₄ (detection limit ~ 2%) nor any other phases are observed (Figure 9a). ²³Na and ⁹³Nb NMR of the unwashed ion-exchanged sample offer an additional level of detail. The ²³Na NMR spectrum of the unwashed sample exhibits a sharp, high-intensity signal from NaNO₃ at -8.0 ppm and then broader intensity from 10 to -20 ppm (Figure 9b). This latter ²³Na signal decreases with ion-exchange time. The ⁹³Nb NMR lineshapes of unwashed samples after 1 min or 12 h of ion exchange do not show noticeable differences (Figure 9c). NMR calculations of L-Na_{*x*}Li_{3-*x*}NbO₄ yielded ²³Na and ⁹³Nb NMR parameters consistent with the experimental spectra (Figure 9b,c, Supplementary Table S4).

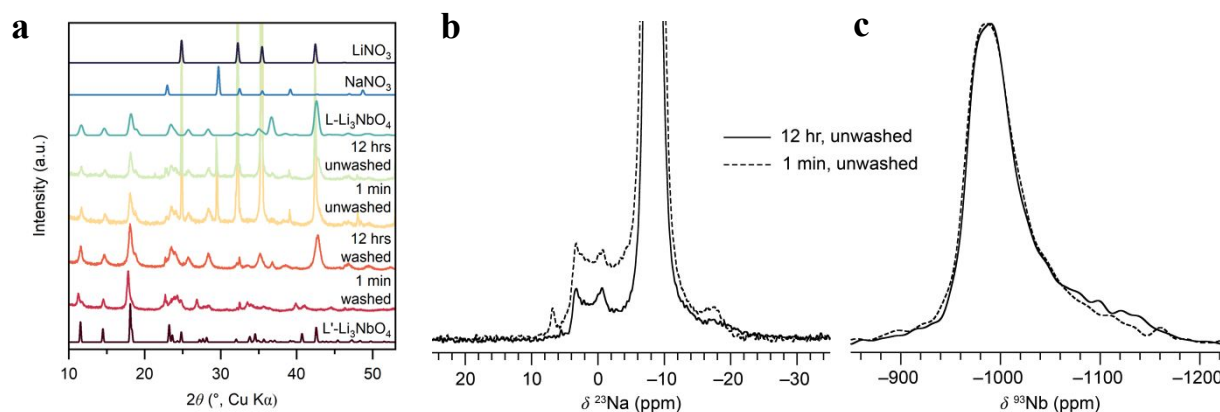


Figure 9. (a) XRD, (b) ^{23}Na and (c) ^{93}Nb NMR of unwashed $\text{L-Li}_3\text{NbO}_4$ after 1 min and 12 h of ion exchange. ^{23}Na and ^{93}Nb NMR measured at 10 and 39 kHz MAS, respectively, and 9.4 T. Spectra are normalized with respect to sample mass and number of scans. The unwashed sample contains a large quantity of LiNO_3 and also NaNO_3 that forms from ion exchange in the flux.

Combining the evidence that (i) residual sodium is present in $\text{L-Li}_3\text{NbO}_4$, especially at short reaction times, (ii) that no sodium (other than precursor NaNbO_3) is observed in the ^{23}Na NMR spectra of the ion-exchange samples after water washing, and (iii) that Na_3NbO_4 is unstable in water, it stands to reason that protons replace the residual sodium in $\text{L-Na}_x\text{Li}_{3-x}\text{NbO}_4$ during the washing process to yield $\text{L-H}_x\text{Li}_{3-x}\text{NbO}_4$. Geometry-optimized DFT structures of all $\text{L-H}_x\text{Li}_{3-x}\text{NbO}_4$ feature hydrogen bonds bridging across two $[\text{Nb}_4\text{O}_{16}]^{12-}$ clusters. DFT NMR calculations of proton-containing $\text{L-H}_x\text{Li}_{3-x}\text{NbO}_4$ tended toward large ^{93}Nb NMR quadrupolar coupling constants (up to > 100 MHz), consistent with the observation that most of the ^{93}Nb signal is “missing” at short timescales (Figure 10, Supplementary Table S5), which is expected of any ^{93}Nb site with C_Q above ~ 50 MHz at 9.4 T.

With this understanding of the secondary ion exchange during the water washing step to remove the flux, we can again consider the time-resolved evolution. Subtle average structure evolution occurs in the diffraction data as a function of ion-exchange reaction times (Figure 8). At short reaction times, XRD from the unwashed and washed samples differ (Figure 8, Figure 9a). However, after 12 h reaction, XRD of washed and unwashed samples are the same, and also match that of the unwashed 1 min phase, which are all consistent with the L- Li_3NbO_4 lattice parameters derived from

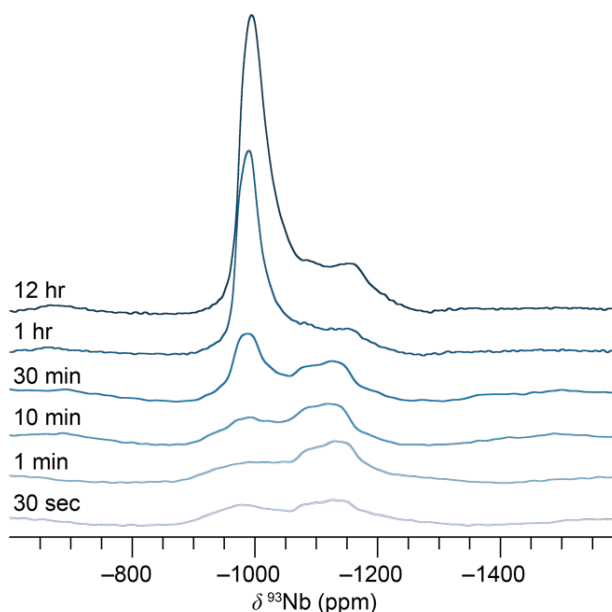


Figure 10. ^{93}Nb NMR of water-washed L- Li_3NbO_4 as a function of ion exchange time at 39 kHz MAS and 9.4 T. Spectra are normalized with respect to sample mass and number of scans.

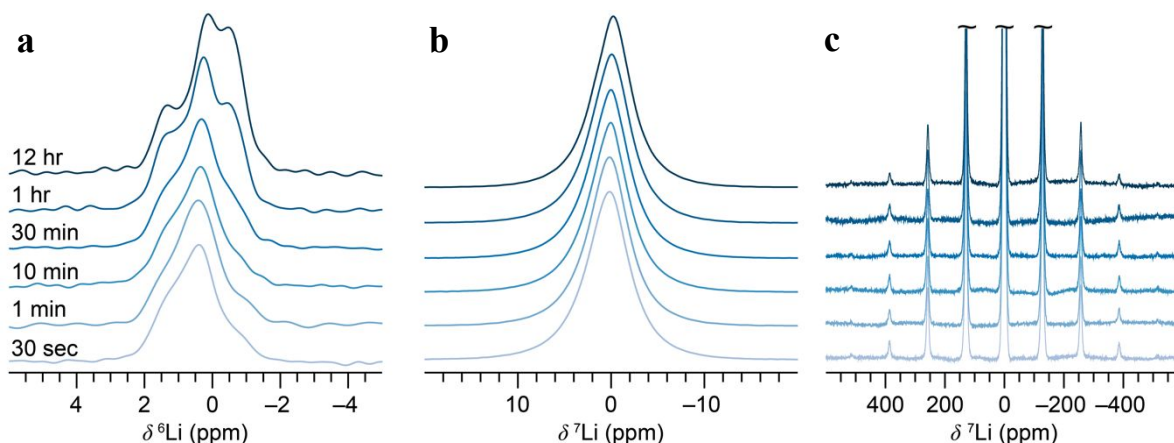


Figure 11. (a) ^7Li centerband, (b) ^7Li sideband manifold, and (c) ^6Li centerband evolution of L- Li_3NbO_4 over the course of the ion exchange reaction. Centerband truncated in (c). Spectra are normalized with respect to sample mass and number of scans.

neutron diffraction data (Table 1). The outlier is the washed sample after short ion-exchange time, which can be refined in the same space group as L- Li_3NbO_4 but with new lattice parameters ($a = 10.674(1) \text{ \AA}$, $b = 12.225(2) \text{ \AA}$, $c = 5.314(4) \text{ \AA}$, $\beta = 112.689(2)^\circ$, vol. = $639.7(2) \text{ \AA}^3$); this phase is denoted L'- Li_3NbO_4 . The L' phase has a 5.4% larger volume and 3.2° larger β angle than the L phase. Taken together, the ^{23}Na NMR and diffraction data suggest that a small fraction of Na remains after short ion exchange. However, as sodium is ion exchanged for protons during the washing step, the structure relaxes substantially to form the L' phase. High-resolution ^6Li NMR of the washed samples reveals that there is some redistribution of

the population of intensity within the same 2 ppm region as a function of ion exchange time, likely related to the lattice and proton compositional evolution (Figure 11a). No changes are observed in the ^7Li centerband or spinning sidebands (Figure 11b,c) and any intensity changes are minor.

Another observation from the ion exchange timescale measurements is that the diffraction peaks are generally sharper at short reaction times (Figure 8a, most easily seen at low 2θ , e.g., $10\text{--}15^\circ$, where there is no peak overlap). This is in contrast to a typical synthesis where crystallinity increases over time. As will be demonstrated in detail in the next section, L- Li_3NbO_4 is a metastable compound and the increase in diffraction line broadening over time indicates increasing strain as the structure tries to convert to the ground-state c- Li_3NbO_4 polymorph.

Variable temperature XRD. The known high-temperature phase of Li_3NbO_4 is cubic with space group $\bar{I}43m$.^{13,49,50} DFT enthalpy calculations return that c- Li_3NbO_4 is 6.6 meV per atom more stable than L- Li_3NbO_4 , a relatively small difference. In order to probe the stability of L- Li_3NbO_4 , samples were heated from 400 to 800 °C for 12 h (Figure 12; n.b., nine different samples heated individually to 400 °C, 450 °C, etc., not one sample ramped up in temperature). Between 550–600 °C, L- Li_3NbO_4 peaks disappeared. Slightly earlier, at 500 °C, an unidentified intermediate started to form with broad intensity at 13.5 and 30.9° 2θ , those reflections narrowed at temperatures up to 650 °C and then disappeared by 750 °C. At 650 °C, reflections from LiNbO_3 appeared, owing to the understoichiometry of lithium in the samples that is consistent with the aforementioned discussion of proton exchange for residual sodium according to: $\text{H}_x\text{Li}_{3-x}\text{NbO}_4 \rightarrow (1-x/2)\text{Li}_3\text{NbO}_4 + x/2\text{LiNbO}_3 + x/2\text{H}_2\text{O}$ upon heating.

Although there is not a group–subgroup relationship between $\bar{I}43m$ and $C2/m$, some of the reflections from c- Li_3NbO_4 and L- Li_3NbO_4 are in very similar positions owing to the similarity of their unit cells which both have $Z = 8$ and volumes of 598.6 Å³ and 606.7 Å³, respectively.

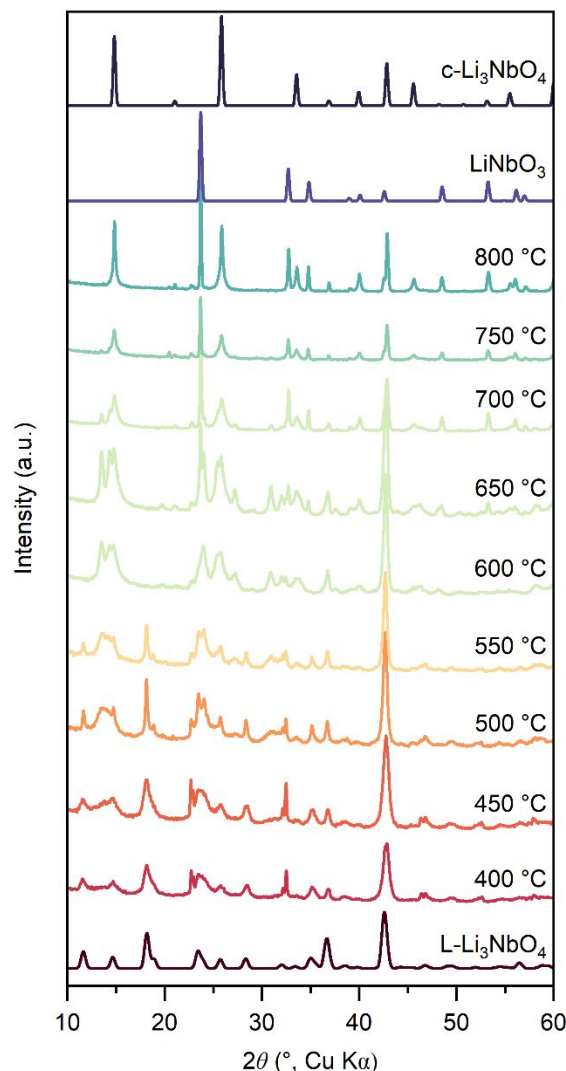


Figure 12. Phase transition of L- Li_3NbO_4 to c- Li_3NbO_4 as a function of temperature.

Extension to L-Na₃TaO₄. Based on the results for L-Li₃NbO₄, an obvious question was whether this methodology could be extended to the tantalum system. The ground state phase L-Na₃TaO₄ is isostructural with L-Na₃NbO₄, while the known lithium-rich tantalates have unique crystal chemistry. Li₃TaO₄ has at least two known polymorphs, α and β , which both comprise kinked chains of edge-sharing TaO₆ octahedra.^{18,20} Ion exchange of L-Na₃TaO₄ in molten lithium nitrate yielded L-Li₃TaO₄ (Figure 13, Table 5). The DFT calculated enthalpy of L-Li₃TaO₄ is 6.8 meV per atom higher than the solid-state synthesized phase β -Li₃TaO₄. The lattice parameters of the ion exchanged phase suggest that some Na⁺ was left in the structure even after 12 h ion exchange, which was subsequently exchanged for H⁺ (Table 5, Supplementary Table 3).

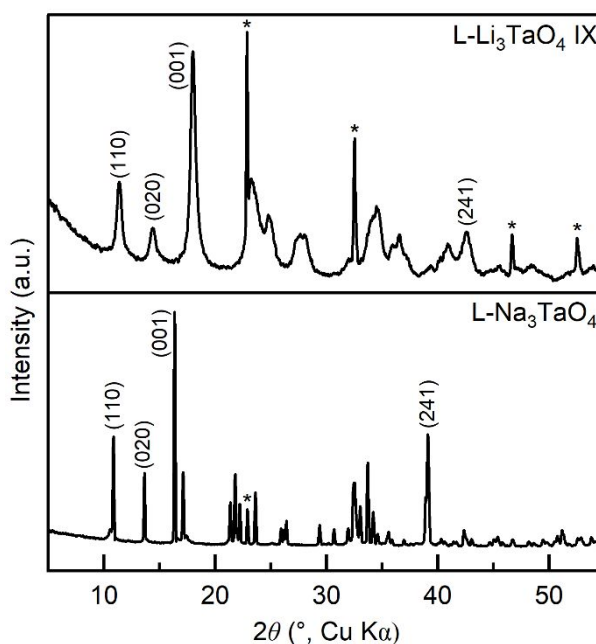


Figure 13. X-ray diffraction patterns of L-Na₃TaO₄ and L-Li₃TaO₄ after 12 h of ion exchange in a molten lithium salt. Some of the most prominent reflections are labeled. Asterisks denote observed NaTaO₃ reflections.

Table 5. Lattice parameters of L-Na₃TaO₄ and L-Li₃TaO₄ from refinement of the structures with laboratory X-ray powder diffraction data.

Layered C2/m	L-Na ₃ TaO ₄	L-Li ₃ TaO ₄	Δ (%)
a (Å)	11.145(3)	10.63(2)	-4.6
b (Å)	13.0044(5)	12.187(4)	-6.3
c (Å)	5.7601(7)	5.316(6)	-7.7
β (°)	109.657(3)	112.22(3)	
Volume (Å ³)	786.21(6)	637.69(3)	-18.9

Experimental ^{23}Na NMR of L- Na_3TaO_4 was in excellent agreement with the spectrum calculated from the structure model (Figure 14a, Table 6). Analogously to the niobium system, a small impurity of NaTaO_3 was observed after the synthesis of L- Na_3TaO_4 and remained present through the ion exchange and washing steps. After lithium ion exchange and water-washing to remove the flux, NaTaO_3 was the only residual ^{23}Na resonance (Figure 14b).⁵¹

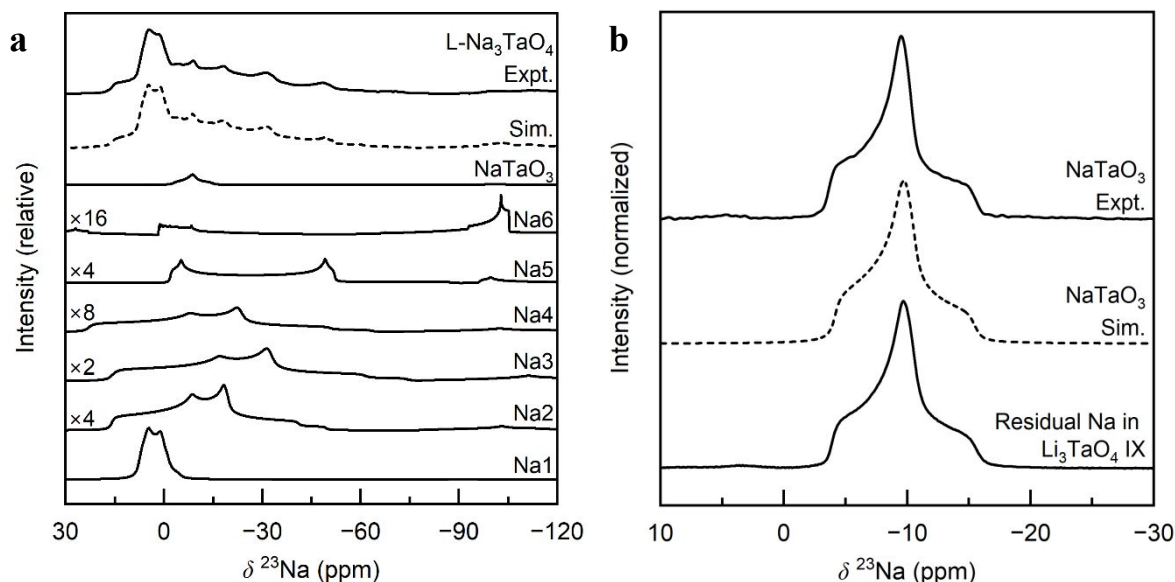


Figure 14. (a) ^{23}Na NMR of L- Na_3TaO_4 . The simulated ^{23}Na spectrum in (a) includes contributions from the six unique sodium sites in the crystal structure and the NaTaO_3 impurity. Broader sites in (a) are scaled up in intensity, as denoted, to better show their lineshapes. (b) Experimental and simulated ^{23}Na spectrum of NaTaO_3 compared to the residual ^{23}Na lineshape observed in L- Li_3TaO_4 after ion exchange.

Table 6. ^{23}Na NMR of Na_3TaO_4 and NaTaO_3 .

Site	calculated					experimental ^a			
	σ_{iso} (ppm)	δ_{aniso} (ppm)	η_{CS}	C_Q (MHz)	η_Q	δ_{iso} (ppm)	C_Q (MHz)	η_Q	
L- Na_3TaO_4	Na1	554.8	11.5	0.14	1.56	0.36	8.7	1.5(1)	0.36(4)
	Na2	546.5	-20.9	0.81	-3.24	0.66	17.2	3.3(2)	0.70(2)
	Na3	544.1	-15.1	0.28	-3.90	0.67	17.3	3.9(2)	0.67(2)
	Na4	542.6	-13.0	0.60	-3.83	0.66	23.8	3.8(2)	0.66(2)
	Na5	550.4	-11.6	0.33	-4.27	0.06	10.8	4.2(2)	0.06(2)
	Na6	549.0	-27.9	0.57	5.82	0.64	n/r	n/r	n/r
NaTaO_3	Na1						-3.5	1.35(1)	0.93(3)

^a‘Experimental’ values obtained by first simulating the GIPAW calculated values and then refining the isotropic chemical shift and the quadrupolar coupling magnitude and asymmetry to obtain a best-fit of the simulation to the experimental data.

^6Li and ^7Li spectra of ion exchanged L- Li_3TaO_4 (Figure 15, Table 7) and solid-state synthesized $\beta\text{-Li}_3\text{TaO}_4$ (Figure 16, Table 7) show distinction only between the ^6Li centerbands. This is consistent with the calculated lithium NMR parameters suggesting a 0.1 ppm chemical shift range for the three lithium sites in $\beta\text{-Li}_3\text{TaO}_4$ and a 1.4 ppm chemical shift range for the six lithium sites in L- Li_3TaO_4 ; whereas both have ^7Li C_Q s ranging from 21–104 kHz.

Table 7. $^{6,7}\text{Li}$ NMR of Li_3TaO_4 .

	Site	σ_{iso} (ppm)	δ_{aniso} (ppm)	η_{CS}	C_Q (kHz) ^a	η_Q
$\beta\text{-Li}_3\text{TaO}_4$	Li1	91.01	1.51	0.8	-20.9	0.97
	Li2	90.92	-1.11	0.59	103.7	0.71
	Li3	90.99	1.38	0.56	25.1	0.64
L- Li_3TaO_4	Li1	90.15	-0.84	0.47	20.8	0.71
	Li2	91.06	3.11	0.97	48.9	0.92
	Li3	90.88	1.22	0.53	62.1	0.52
	Li4	91.55	2.08	0.91	-65.7	0.01
	Li5	90.99	1.24	0.39	52.6	0.28
	Li6	90.66	3.18	0.32	-104.3	0.58

^a C_Q for ^7Li nucleus. ^6Li C_Q s are scaled by $Q(^6\text{Li})/Q(^7\text{Li}) = 0.808/40.1$.⁴⁸

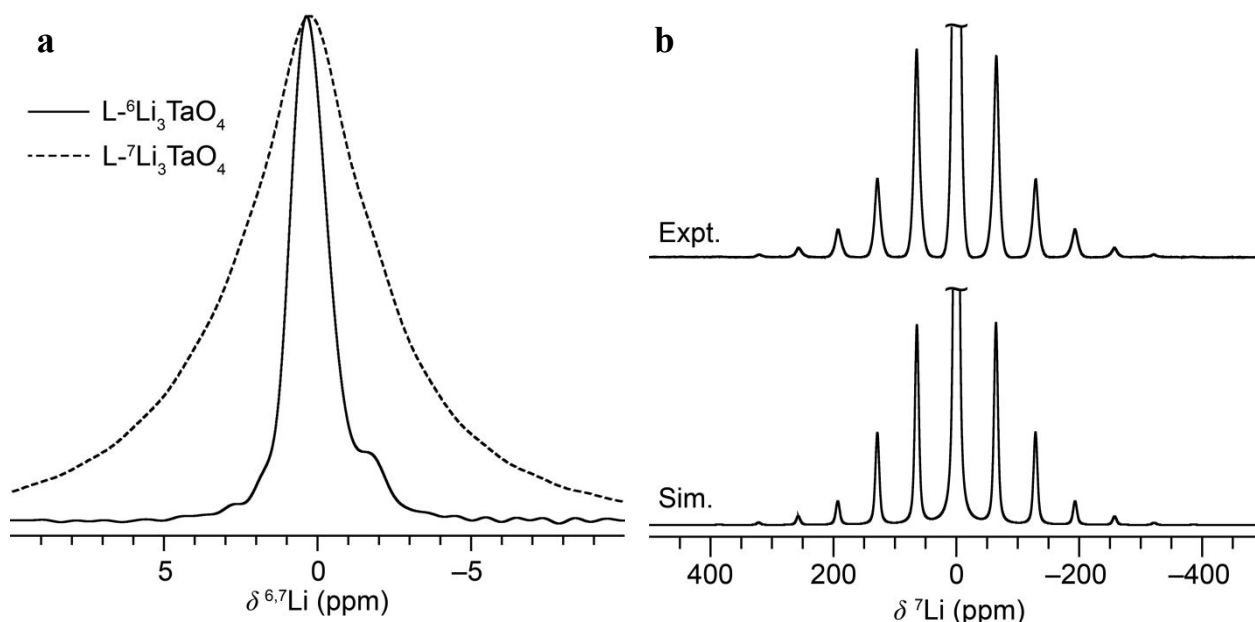


Figure 15. (a) $^{6,7}\text{Li}$ centerband spectra and (b) ^7Li spinning sideband manifold of L- Li_3TaO_4 at 9.4 T and 10 kHz MAS. Spectra in (a) are intensity normalized. Centerband truncated in (b). Sideband simulation performed with the calculated ^7Li C_Q and η_Q parameters for L- Li_3TaO_4 .

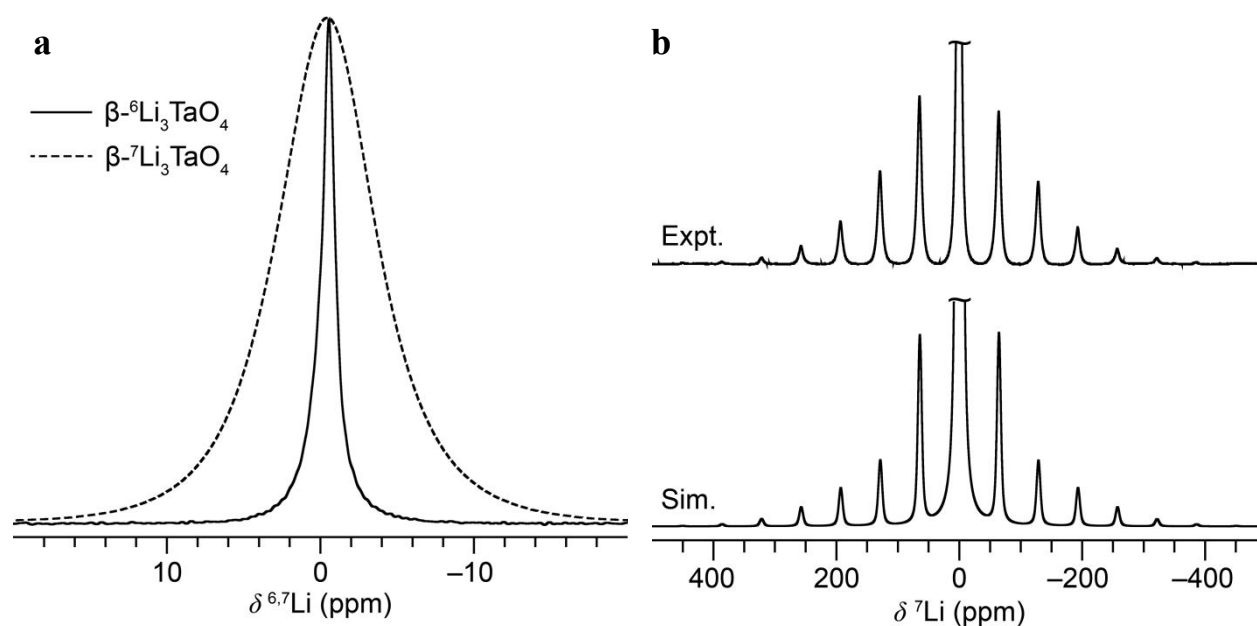


Figure 16. (a) $^{6,7}\text{Li}$ centerband spectra and (b) ^7Li spinning sideband manifold of $\beta\text{-Li}_3\text{TaO}_4$ at 9.4 T and 10 kHz MAS. Spectra in (a) are intensity normalized. Centerband truncated in (b). Sideband simulation performed with the calculated ^7Li C_Q and η_Q parameters for $\beta\text{-Li}_3\text{TaO}_4$.

Owing to the instability of Na_3NbO_4 and Na_3TaO_4 in water, conventional ambient temperature aqueous ion exchange reactions in these systems are not possible. However, preliminary tests indicate that non-aqueous ion exchange at 22 °C is possible, which is a future direction to explore proton-free lithium-rich niobates and tantalates. Given their layered structures, it would also be interesting to explore the Li^+ conductivity of these phases, which, together with electrochemical stability studies, would help establish the relevance of these new materials as solid electrolytes in solid-state batteries.

Conclusions

Two new lithium-rich early transition metal oxides with layered structures and non-close-packed oxygen atoms— $\text{L-Li}_3\text{NbO}_4$ and $\text{L-Li}_3\text{TaO}_4$ —have been synthesized via molten salt ion exchange chemistry. Topotactic exchange occurred despite that the volume change is ca. 20% and that the basic building units of layered Na_3MO_4 ($M = \text{Nb}, \text{Ta}$) are 0D clusters. X-ray and neutron diffraction, $^{6,7}\text{Li}$, ^{23}Na , and ^{93}Nb solid-state NMR, and DFT calculations were combined to provide a detailed look at the crystal chemistry and transformation process. Time-stepped measurements revealed that some Na^+ remains, which gets replaced by H^+ during the washing process that removes the salt flux. As a function of ion exchange time, ^{93}Nb NMR lineshapes sharpen while diffraction reflections broaden. This difference in the local and long-range structure evolution can be attributed to the different broadening mechanisms: ^{93}Nb C_Q s increase when H^+ is present (H^+ decreases with time) while XRD peaks broaden because the

structure is metastable and wants to transform to $c\text{-Li}_3\text{NbO}_4$ (strain increases with time). Coplanar octahedra in the $[\text{Nb}_4\text{O}_{16}]^{12-}$ cluster in $L\text{-Li}_3\text{NbO}_4$ transform into the supertetrahedral arrangement in $c\text{-Li}_3\text{NbO}_4$ above 550 °C. Residual protons in $L\text{-Li}_3\text{NbO}_4$ represent a lithium deficiency that lead to the formation of LiNbO_3 upon heating. Soft-chemical synthesis together with NMR crystallography is a powerful combination for the realization and detailed understanding of new metastable materials in compositional phase spaces such as lithium-rich metal oxides that have proven difficult to access and characterize owing to the large quantity of light alkali elements and/or the presence and role of protons. A more general takeaway is that topotactic ion exchange of non-framework structures, even with extremely large volume changes, is not only possible but can be a rapid route to produce new compounds.

Associated Content

T_1 relaxation data, NMR measurement details, additional diffraction and NMR data, scanning electron microscopy images, particle size distributions, calculated parameters of mixed H/Li/Na phases.

CCDC Depositions: 2361250–2361253

Raw data and metadata: Ko, Sarah L.; Dorrell, Jordan A.; Morris, Andrew J.; Griffith, Kent J. (2024). Data from: Metastable Layered Lithium-rich Niobium and Tantalum Oxides via Nearly Instantaneous Cation Exchange. UC San Diego Library Digital Collections. <https://doi.org/10.6075/J0CV4J0M>

Corresponding Author

Email: k3griffith@ucsd.edu

Notes

The authors declare no competing financial interest.

Acknowledgements

Neutron diffraction measurements were performed at ORNL's Spallation Neutron Source, sponsored by the Scientific User Facilities Division, Office of Basic Energy Sciences, U.S. Department of Energy. The authors thank ORNL beamline scientist Dr. Alicia Manjón-Sanz for performing the neutron diffraction experiments.

References

- 1 M. Zhang, D. A. Kitchaev, Z. Lebens-Higgins, J. Vinckeviciute, M. Zuba, P. J. Reeves, C. P. Grey, M. S. Whittingham, L. F. J. Piper, A. Van Der Ven and Y. S. Meng, *Nat. Rev. Mater.*, 2022, **7**, 522–540.
- 2 A. Gutierrez, D. Tewari, J. Chen, V. Srinivasan, M. Balasubramanian and J. R. Croy, *J. Electrochem. Soc.*, 2023, **170**, 030509.
- 3 P. Zhong, B. Deng, T. He, Z. Lun and G. Ceder, *Joule*, 2024, S2542435124001454.
- 4 R. Fong, N. Mubarak, S. Park, G. Lazaris, Y. Liu, R. Malik, D. Seo and J. Lee, *Adv. Energy Mater.*, 2024, 2400402.
- 5 N. Yabuuchi, *Curr. Op. Electrochem.*, 2022, **34**, 100978.
- 6 H. Liu, Z. Zhu, Q. Yan, S. Yu, X. He, Y. Chen, R. Zhang, L. Ma, T. Liu, M. Li, R. Lin, Y. Chen, Y. Li, X. Xing, Y. Choi, L. Gao, H. S. Cho, K. An, J. Feng, R. Kostecki, K. Amine, T. Wu, J. Lu, H. L. Xin, S. P. Ong and P. Liu, *Nature*, 2020, **585**, 63–67.
- 7 P. Barnes, Y. Zuo, K. Dixon, D. Hou, S. Lee, Z. Ma, J. G. Connell, H. Zhou, C. Deng, K. Smith, E. Gabriel, Y. Liu, O. O. Maryon, P. H. Davis, H. Zhu, Y. Du, J. Qi, Z. Zhu, C. Chen, Z. Zhu, Y. Zhou, P. J. Simmonds, A. E. Briggs, D. Schwartz, S. P. Ong and H. Xiong, *Nat. Mater.*, 2022, **21**, 795–803.
- 8 Q. Jacquet, G. Rouse, A. Iadecola, M. Saubanère, M.-L. Doublet and J.-M. Tarascon, *Chem. Mater.*, 2018, **30**, 392–402.
- 9 D. R. Modeshia, R. I. Walton, M. R. Mitchell and S. E. Ashbrook, *Dalton Trans.*, 2010, **39**, 6031.
- 10 G. C. Mather, C. Dussarrat, J. Etourneau and A. R. West, *J. Mater. Chem.*, 2000, **10**, 2219–2230.
- 11 J. F. Dorrian and R. E. Newnham, *Mater. Res. Bull.*, 1969, **4**, 179–183.
- 12 K. Ukei, H. Suzuki, T. Shishido and T. Fukuda, *Acta Cryst. C*, 1994, **50**, 655–656.
- 13 T. Shishido, H. Suzuki, K. Ukei, T. Hibiya and T. Fukuda, *J. Alloys Compd.*, 1996, **234**, 256–259.
- 14 G. Blasse, *Zeitschrift anorg allge chemie*, 1964, **331**, 44–50.
- 15 C. D. Whiston and A. J. Smith, *Acta Cryst.*, 1965, **19**, 169–173.
- 16 Y. Bouillaud, *Bull. Soc. Chim. France*, 1965, **11**, 519–525.
- 17 J. Darriet and J. Galy, *Bull. Soc. fr. Minéral. Cristallogr.*, 1974, **97**, 3–5.
- 18 M. Zocchi, M. Gatti, A. Santoro and R. S. Roth, *J. Solid State Chem.*, 1983, **48**, 420–430.
- 19 D. Du Boulay, A. Sakaguchi, K. Suda and N. Ishizawa, *Acta Cryst. E*, 2003, **59**, i80–i82.
- 20 R. S. Roth, *J. Solid State Chem.*, 1984, **51**, 403–404.
- 21 M.-C. Illy, A. L. Smith, G. Wallez, P. E. Raison, R. Caciuffo and R. J. M. Konings, *J. Nucl. Mater.*, 2017, **490**, 101–107.
- 22 M. R. Cosby, G. S. Mattei, Y. Wang, Z. Li, N. Bechtold, K. W. Chapman and P. G. Khalifah, *J. Phys. Chem. C*, 2020, **124**, 6522–6527.
- 23 A. Clearfield, *Chem. Rev.*, 1988, **88**, 125–148.
- 24 J. Bréger, K. Kang, J. Cabana, G. Ceder and C. P. Grey, *J. Mater. Chem.*, 2007, **17**, 3167.

- 25 L. Karger, D. Weber, D. Goonetilleke, A. Mazilkin, H. Li, R. Zhang, Y. Ma, S. Indris, A. Kondrakov, J. Janek and T. Brezesinski, *Chem. Mater.*, 2023, **35**, 648–657.
- 26 H. Gwon, S.-W. Kim, Y.-U. Park, J. Hong, G. Ceder, S. Jeon and K. Kang, *Inorg. Chem.*, 2014, **53**, 8083–8087.
- 27 Y. Luo, Q. Pan, H. Wei, Y. Huang, L. Tang, Z. Wang, C. Yan, J. Mao, K. Dai, Q. Wu, X. Zhang and J. Zheng, *Adv. Energy Mater.*, 2023, **13**, 2300125.
- 28 M. A. Bizeto and V. R. L. Constantino, *Mater. Res. Bull.*, 2004, **39**, 1729–1736.
- 29 S. Uchida, *Chem. Sci.*, 2019, **10**, 7670–7679.
- 30 M. G. Barker and D. J. Wood, *J. Chem. Soc., Dalton Trans.*, 1972, 9–13.
- 31 A. Huq, M. Kirkham, P. F. Peterson, J. P. Hodges, P. S. Whitfield, K. Page, T. Hugle, E. B. Iverson, A. Parizzi and G. Rennich, *J. Appl. Cryst.*, 2019, **52**, 1189–1201.
- 32 B. H. Toby and R. B. Von Dreele, *J. Appl. Cryst.*, 2013, **46**, 544–549.
- 33 T. Kinoshita, *Adv. Powder Tech.*, 2001, **12**, 589–602.
- 34 D. Massiot, F. Fayon, M. Capron, I. King, S. Le Calvé, B. Alonso, J. Durand, B. Bujoli, Z. Gan and G. Hoatson, *Magn. Reson. Chem.*, 2002, **40**, 70–76.
- 35 S. Sturniolo, T. F. G. Green, R. M. Hanson, M. Zilka, K. Refson, P. Hodgkinson, S. P. Brown and J. R. Yates, *Solid State Nucl. Magn. Reson.*, 2016, **78**, 64–70.
- 36 R. K. Harris, E. D. Becker, R. Goodfellow and P. Granger, *Pure Appl. Chem.*.
- 37 J.-P. Amoureux, C. Fernandez and S. Steuernagel, *J. Magn. Reson., Series A*, 1996, **123**, 116–118.
- 38 S. Hayashi and K. Hayamizu, *Bull. Chem. Soc. Japan*, 2006, **62**, 2429–2430.
- 39 K. J. Pike, R. P. Malde, S. E. Ashbrook, J. McManus and S. Wimperis, *Solid State Nucl. Magn. Reson.*, 2000, **16**, 203–215.
- 40 S. Prasad, P. Zhao, J. Huang, J. J. Fitzgerald and J. S. Shore, *Solid State Nucl. Magn. Reson.*, 2001, **19**, 45–62.
- 41 S. J. Clark, M. D. Segall, C. J. Pickard, P. J. Hasnip, M. I. J. Probert, K. Refson and M. C. Payne, *Zeitschrift für Kristallographie – Cryst. Mater.*, 2005, **220**, 567–570.
- 42 C. J. Pickard and F. Mauri, *Phys. Rev. B*, 2001, **63**, 245101.
- 43 H. J. Monkhorst and J. D. Pack, *Phys. Rev. B*, 1976, **13**, 5188–5192.
- 44 J. D. Pack and H. J. Monkhorst, *Phys. Rev. B*, 1977, **16**, 1748–1749.
- 45 W. I. F. David, *Structure Determination from Powder Diffraction Data*, Oxford University Press, 2002.
- 46 K. E. Johnston, C. C. Tang, J. E. Parker, K. S. Knight, P. Lightfoot and S. E. Ashbrook, *J. Am. Chem. Soc.*, 2010, **132**, 8732–8746.
- 47 J. Goodenough and J. Longo, *Landolt-Börnstein Numerical Data and Functional Relationships in Science and Technology, New Series. Group III: Crystal and Solid State Physics*, 1970, **4**, 207–262.
- 48 P. Pyykkö, *Mol. Phys.*, 2018, **116**, 1328–1338.
- 49 G. Blasse, *Z. anorg. allg. Chem.*, 1963, **326**, 44–46.
- 50 J.-C. Grenier and G. Bassi, *Bulletin de Minéralogie*, 1965, **88**, 345–346.
- 51 S. E. Ashbrook, L. Le Pollès, R. Gautier, C. J. Pickard and R. I. Walton, *Phys. Chem. Chem. Phys.*, 2006, **8**, 3423–3431.

Data availability statement is in main text as:

CCDC Depositions: 2361250–2361253

Raw data and metadata: Ko, Sarah L.; Dorrell, Jordan A.; Morris, Andrew J.; Griffith, Kent J. (2024). Data from: Metastable Layered Lithium-rich Niobium and Tantalum Oxides via Nearly Instantaneous Cation Exchange. UC San Diego Library Digital Collections. <https://doi.org/10.6075/J0CV4J0M>